

3D self-organized microvascular model of the human blood-brain barrier with endothelial cells, pericytes and astrocytes

*Original*

3D self-organized microvascular model of the human blood-brain barrier with endothelial cells, pericytes and astrocytes / Campisi, M., Shin, Y., Osaki, T., Hajal, C., Chiono, V., Kamm, R.D.. - In: BIOMATERIALS. - ISSN 0142-9612. - ELETTRONICO. - 180:(2018), pp. 117-129. [10.1016/j.biomaterials.2018.07.014]

*Availability:*

This version is available at: 11583/2716982 since: 2018-11-10T16:56:49Z

*Publisher:*

Elsevier Ltd

*Published*

DOI:10.1016/j.biomaterials.2018.07.014

*Terms of use:*

This article is made available under terms and conditions as specified in the corresponding bibliographic description in the repository

*Publisher copyright*

Elsevier postprint/Author's Accepted Manuscript

© 2018. This manuscript version is made available under the CC-BY-NC-ND 4.0 license  
<http://creativecommons.org/licenses/by-nc-nd/4.0/>. The final authenticated version is available online at:  
<http://dx.doi.org/10.1016/j.biomaterials.2018.07.014>

(Article begins on next page)



34 with permeability lower than conventional *in vitro* models, and similar to *in vivo* measurements in rat  
35 brain. This robust and physiologically relevant BBB microvascular model offers an innovative and  
36 valuable platform for drug discovery to predict neuro-therapeutic transport efficacy in pre-clinical  
37 applications as well as recapitulate patient-specific and pathological neurovascular functions in  
38 neurodegenerative disease.

39

## 40 Introduction

41  
42 The blood-brain barrier (BBB) and blood-spinal cord barrier help maintain brain homeostasis [1] by  
43 regulating the transport of necessary nutrients, ions, and hormones, while preventing the entry of  
44 neurotoxins or pathogens into the brain owing to a complex membrane transport mechanism [2]. The  
45 BBB consists of specialized endothelial cells (ECs) interconnected by junctional complexes including  
46 tight junctions (TJs) and adherens junctions, surrounded by pericytes (PCs) and astrocytes (ACs), and  
47 ensheathed in a basal lamina. Each of these specialized features contributes to BBB integrity, and to  
48 the control of transport processes [3]. Loss of BBB integrity is associated with Alzheimer's disease  
49 [4][5], Parkinson's disease [6], and multiple sclerosis [7], as well as with brain cancer [8].  
50 Furthermore, the BBB regulates active and passive transport of solutes into the brain [9][10], posing  
51 an obstacle to drug delivery for the treatment of neurological diseases and brain tumors [11][12].

52  
53 For these reasons, preclinical models of the BBB are developed to understand its role in the  
54 pathogenesis of neurological diseases as well as to evaluate drug permeability. For years, *in vivo*  
55 animal models have been used to model the BBB and study drug delivery [13]. Although these  
56 techniques are considered the gold standard, 80% of successful drug candidates in animal models  
57 later failed in clinical trials [14][15].

58  
59 To optimize the design of innovative therapies and drug carriers, a robust, reliable, and cost-effective  
60 *in vitro* BBB model that adequately reflects human *in vivo* conditions is required [16][17]. For several  
61 decades, transwell assays have been widely adopted to assess drug permeability by culturing a  
62 confluent monolayer of ECs in the absence or presence of PCs or ACs [18]. Although this system is  
63 reproducible and easy to use, it has limitations in mimicking fundamental BBB features and  
64 microenvironmental complexities such as cell-cell or cell-matrix interactions, compromising its  
65 ability to accurately model brain capillaries in terms of junctional proteins and membrane transporter

66 expression [17][19][20]. Recently, BBB spheroids have been developed to study organogenesis and  
67 the transport of brain penetrating agents [21][22]. Although these systems are cost-effective, they are  
68 limited in their ability to recreate a realistic and relevant BBB morphology. As an alternative to  
69 simple culture models, microfluidic technology offers a promising tool for reconstituting the BBB  
70 with several advantages: microfluidic systems allow for precise control of the 3D cellular and  
71 extracellular matrix (ECM) microenvironment, while providing a platform for the study of cellular  
72 and structural responses to various stimuli. These systems mimic the complex cellular interactions  
73 and structures found in many tissues or organs *in vivo*, and are thus referred to as 'organ-on-a-chip'  
74 [23][24]. Recently, efforts to reconstitute a 3D BBB model within a microfluidic system have  
75 accelerated with the development of organ-on-a-chip assays to study immune cell transmigration [25],  
76 metastatic cancer extravasation to the brain [26], as well as vessel formation in a tubular shape [27].  
77 However, systems to date have relatively large diameters (~ 600-800  $\mu\text{m}$ ) [27] compared to the  
78 dimension of human BBB vasculature *in vivo* (arterioles and venules 10-100  $\mu\text{m}$ ; capillaries 7-10  
79  $\mu\text{m}$ ) [28][29], and fail to recapitulate BBB microvasculature morphology and development in terms  
80 of mature cell-cell interactions via natural biological processes, as well as physiological blood flow  
81 rates and wall shear stresses needed to activate mechanosensing/mechanotransduction pathways, thus  
82 altering realistic transport exchange mechanisms at the level of brain capillaries [30][31].

83

84 Two microfluidic models have been recently reported using a co-culture of human ECs and rat  
85 neurons and ACs. One incorporated a compartmentalized 3D monolayer of human cerebral  
86 microvascular ECs in co-culture with primary rat ACs and neurons [32]. In a separate study, similar  
87 to the previous model [33], a BBB microvascular network ( $\mu\text{VN}$ ) platform created by a  
88 vasculogenesis-like process, culturing human umbilical vein endothelial cells (HUVECs) in a 3D  
89 ECM-mimetic hydrogel showed that direct interaction with neural tissue from the rat cortex was  
90 responsible for the low permeability values measured [34].

91

92 However, while co-cultures with cells from different species are advantageous in terms of  
93 accessibility and ease of genetic manipulations, cross-species compatibility remains a concern  
94 regarding the relevance of these results to human physiology [35]. Moreover, HUVECs offer a poor  
95 model for cerebral vasculature, while PCs, recognized to be a key component of the BBB [35], have  
96 not been considered in these models [32][34].

97

98 To address the main limitations of the current state-of-the-art models, we reasoned that a BBB model  
99 developed from human cells co-cultured in a 3D microenvironment would better replicate the human  
100 BBB, based on the hypothesis that the co-culture arrangement could support the maturation and  
101 differentiation of human iPSC cell-derived endothelial cells (iPSC-ECs) into BBB microvascular cells.  
102 Hence, a 3D BBB microfluidic model was designed consisting of self-assembled  $\mu$ VNs from human  
103 iPSC-ECs as well as human primary brain PCs, and human primary ACs, where all cell types  
104 spontaneously assembled into a modular organization reproducing the BBB structure being in  
105 dynamic and direct contact with each other.

106

107 BBB functionality was evaluated by progressive increase of co-culture complexity up to a tri-culture  
108 of iPSC-ECs, PCs, and ACs. Confocal imaging and immunocytochemistry, permeability  
109 measurements and gene expression analysis were used to quantitatively assess BBB characteristics.  
110 Such human 3D BBB model has unique biological features, representing a promising platform for *in*  
111 *vitro* preclinical experimentation.

112

## 113 **Materials and methods**

114

### 115 **Fabrication of the microfluidic device (micro-device/macro-device)**

116 The 3D microfluidic systems were composed of polydimethylsiloxane (PDMS; Sylgard 184; Dow  
117 Corning, MI, USA) with a single layer microchannel and two fluid channels, fabricated by soft  
118 lithography [36] (Fig. 1c, Supplementary Fig. 1a-b). Elastomer and curing agent were mixed (10:1  
119 volume ratio), degassed and poured onto a silicon master and cured overnight at 60°C. I/O holes were  
120 created with biopsy punches, then the device was taped to remove dust and sterilized as previously  
121 described [37]. The PDMS micro and macro-devices were treated with oxygen plasma (Harrick  
122 Plasma), then bonded to a glass coverslip (Fisher Scientific) coated with poly(D-lysine  
123 hydrobromide) (PDL, Sigma-Aldrich) solution (1 mg/ml) and, finally, placed in an incubator for 3 h  
124 at 37°C, rinsed 3 times and dried overnight.

125

### 126 **Cell culture and device seeding of BBB self-assembled vascular network model**

127 Human iPSC-ECs (Cellular Dynamics International, CDI) were subcultured on flasks coated with  
128 human fibronectin (30 µg/ml, Millipore) in vascular medium (Vasculife VEGF Medium Complete  
129 Kit, icell media supplement, CDI). Pericytes and astrocytes isolated from human brain (ScienCell),  
130 were cultured in growth medium (ScienCell) on a poly-L-lysine (Sigma-Aldrich) coated flask, and  
131 maintained in a humidified incubator (37 °C, 5% CO<sub>2</sub>), replacing the medium every 2 days. Cells  
132 were detached using TrypLE (for iPSC-ECs) and 0.025% trypsin/EDTA for other cell types (Thermo  
133 Fisher). Experiments were performed between passages 3 and 5 for all cells.

134

135 Fibrinogen (6 mg/ml) and thrombin (100 U/ml) from bovine plasma (Sigma-Aldrich) were separately  
136 dissolved in sterile PBS. Then, thrombin was mixed with 1ml of EGM-2 MV (Lonza) and placed on  
137 ice. Cells were detached and spun down at 1200 rpm for 5 min and cell pellet was resuspended in  
138 EGM-2 MV 4 U/ml thrombin. Cell suspension was mixed with fibrinogen (final concentration 3

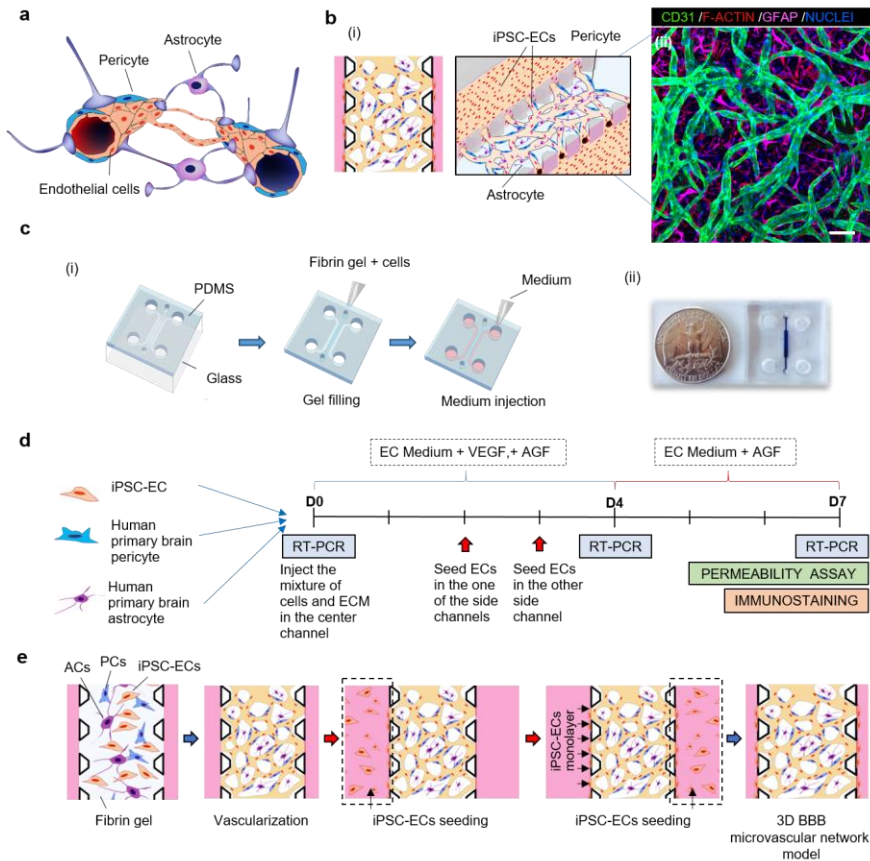
139 mg/ml) at 1:1 volume ratio. The mixture was quickly pipetted into the gel filling ports. Devices were  
140 placed in a humidified enclosure and allowed to polymerize at room temperature (RT) for 15 min  
141 before the fresh medium was introduced to fluidic channels. iPSC-ECs medium was supplemented  
142 with 50 ng/ml of vascular endothelial growth factor (VEGF, Peprotech), for the first four days of  
143 culture. Medium for the tri-culture condition was supplemented with 1% (vol/vol) Astrocyte Growth  
144 factor (AGF, astrocyte growth supplement, ScienCell).

145

146 Three different cell combinations were tested: 1) iPSC-ECs mono-culture ( $6 \times 10^6$  cells/ml), 2) co-  
147 culture iPSC-ECs+PCs (add  $2 \times 10^6$  cells/ml PCs) and 3) tri-culture of iPSC-ECs+PCs+ACs (add  
148  $2 \times 10^6$  cells/ml ACs). After fibrin polymerization, medium channels were coated for 30 min in an  
149 incubator ( $37^\circ\text{C}$  5%  $\text{CO}_2$ ) with human fibronectin ( $60 \mu\text{g/ml}$ ) to promote endothelial cell adhesion.  
150 In each case, iPSC-ECs were subsequently seeded at  $2 \times 10^6$  cells/ml in EBM-2 (Lonza) into the fluidic  
151 channels to reduce diffusion of fluorescent dyes into the gel. Non-adherent cells were removed after  
152 2 h. The device was kept in an incubator for 7 days ( $37^\circ\text{C}$ , 5%  $\text{CO}_2$ ),  $200 \mu\text{l}$  of medium was replaced  
153 every 24 h. Devices prepared in this manner were used for both permeability measurements and  
154 immunocytochemical staining. PC conditioned medium was collected after 3 days, from a T75 flask  
155 of PCs culture, mixed 1:1 volume ratio with fresh medium and replaced every 24 h in the iPSC-ECs  
156 mono-culture in the microfluidic device.

157

158 The *in vitro* BBB model was developed by co-culturing human iPSC-ECs, and human brain PCs and  
159 ACs to mimic certain aspects of the organization and structure of the brain microcirculation observed  
160 *in vivo* (Fig. 1a,b). The BBB model formed by a vasculogenesis-like process, consisted of a well-  
161 connected and perfusable  $\mu\text{VN}$  in a microfluidic device (Fig. 1c, Supplementary Fig. 1a), interacting  
162 via paracrine, juxtacrine and mechanical signaling[38][39]. iPSC-ECs seeded in the side media  
163 channels reduced leakage through the side walls of the central gel region and promoted the formation  
164 of patent vessel connections to the media channels, facilitating flow into the network (Fig. 1d,e).



165

166 **Figure 1: Blood-brain barrier and *in vitro* microvascular network model.** (a) Schematic  
 167 representation of the blood-brain barrier (BBB), composed of brain Endothelial cells (ECs) vessels  
 168 overlapped by pericytes (PCs) and astrocytes (ACs) endfeet. (b, (i)) Schematic representation of  
 169 proposed 3D BBB microvascular network ( $\mu$ VN) model that mimics the microvascular structure  
 170 present in the brain environment. (b, (ii)) Confocal image of self-assembled BBB  $\mu$ VN model  
 171 including iPSC-ECs (CD31, green), PCs (F-actin, red) and ACs (GFAP, magenta), and nuclei (DAPI,  
 172 blue). (c) Microfluidic device fabrication: (c, (i)) PDMS mold with patterned channels were produced  
 173 by soft lithography and bonded to a glass coverslip. The central gel region contained cells and  
 174 hydrogels, side channels and reservoirs were filled with cell culture medium. (c, (ii)) A photo of the  
 175 microfluidic device. (d) Timeline of the experiments. (e) Cell seeding configuration and experimental  
 176 steps of vasculogenesis process of BBB  $\mu$ VN model including iPSC-ECs+PCs+ACs as self-  
 177 assembled microvascular network and 3-dimensional ECs layer covering top, bottom and side  
 178 surfaces of the fluidic channel. Scale bar (b, (ii)) indicates 100  $\mu$ m.

179

180 **Immunocytochemistry and confocal imaging**

181 The 3D BBB  $\mu$ VNs were cultured for 7 days followed by rinsing in PBS and fixation in 4%  
182 paraformaldehyde (PFA, Electron Microscopy Sciences) for 15 min at RT. Cell membranes were  
183 permeabilized with 0.1% Triton X-100 (Sigma-Aldrich) for 5 min at RT and washed twice with PBS.  
184 Primary antibodies (1:100, volume ratio) against CD31, Glial Fibrillary Acidic Protein (GFAP),  
185 (Abcam), F-actin (Rhodamine Phalloidin, Molecular Probes), 4',6-Diamidino-2-Phenylindole (DAPI  
186 Thermo Fisher Scientific), were used to identify, respectively, iPSC-ECs, ACs, PCs, and nuclei.

187 **F-actin is strongly expressed in all cells present in our model, whereas only iPSC-ECs highly express**  
188 **CD31 and only astrocytes express GFAP. We therefore used double staining of CD31/F-actin to**  
189 **identify iPSC-ECs and GFAP/F-actin to identify ACs, which enabled us to clearly identify the PC**  
190 **population as those cells that only express F-actin.**

191 To characterize the presence of TJs and ECM proteins by immunocytochemistry, primary antibodies  
192 were used against: ZO-1 (Invitrogen), occludin, claudin-5, laminin and collagen IV (Abcam).  
193 Secondary antibodies (1:200, volume ratio) were anti-rabbit or anti-mouse IgG conjugated with Alexa  
194 Fluor (488-555, or 647) (Invitrogen). Detail on primary and secondary antibodies are listed in  
195 Supplementary Table 2. Devices were incubated with primary and secondary antibodies overnight at  
196 4°C, placed on a shaker. After PBS washing, devices were imaged using a confocal laser scanning  
197 microscope (FMV-1000, Olympus, Japan) **(aspect ratio 1024×1024) high resolution images at**  
198 **10us/pixel scan velocity.** Phase contrast imaging was used for morphological observations at different  
199 culture time-points (Axiovert 200, Zeiss, Germany). Post-processing and stitching for tiled images  
200 were performed using Imaris (Bitplane, Switzerland) and Fluoview (Olympus, Japan). Fold change  
201 average immunofluorescent (IF) intensity (relative to iPSC-ECs) was calculated by dividing total  
202 immunofluorescent intensity by cell boundary length (ZO-1, occludin, and claudin-5) or by  
203 vascularized area (laminin, collagen IV). ROIs were selected to contain only microvascular portions  
204 such that no part outside the vessels were included in the computations.

205

#### 206 **Characterization of BBB microvascular parameters**

207 To characterize microvascular parameters, confocal images were analyzed using ImageJ software  
208 (<http://rsbweb.nih.gov/ij/>) and plugins (Trainable Weka Segmentation 3D, 3D geometrical measure).

209 Briefly, raw images were prepared by enhancing contrast and removing noise. An automatic threshold  
210 was used to produce binarized images. From 2D projections, lateral vessel area ( $A_{lateral}$ ), and total  
211 branch length ( $L_{branch}$ ) were computed by ImageJ. Percentage of area coverage was calculated  
212 dividing  $A_{lateral}$  by the entire area of the region of interest. Taking advantage of the observation that  
213 most vessels are oriented in a plane parallel to the glass substrate, lateral diameters, parallel to the  
214 glass substrates of the devices, were computed as the ratio of the projected lateral vessel area to the  
215 total branch length. Transverse diameters, perpendicular to the glass substrate, were computed using  
216 the 3D vessel volume ( $V$ ) and the surface area of the vessels in 3D ( $A_{surface}$ ). Average cross-section  
217 area and circularity were computed using lateral and transverse diameters. The sequences of  
218 instructions and equations used to compute both diameters, cross-section, lateral and surface areas  
219 and circularity are shown in Supplementary methods.

220

#### 221 **Microvascular network perfusion and fluorescent dextran-based permeability assay**

222 To assess permeability of the 3D BBB model, solutions containing 10 or 40 kDa FITC-dextran  
223 (Sigma-Aldrich) were introduced as fluorescent tracers, and time-sequential images to assess leakage  
224 through the microvascular barrier were captured. Briefly, after 7 days of culture, each device was  
225 moved to the confocal conditioning chamber (37°C, 5% CO<sub>2</sub>), culture medium was aspirated from  
226 all reservoirs in each side channel. Then, 5 µl of dextran solution in PBS was injected in one side,  
227 simultaneously with 5 µl of medium on the other fluidic channel to maintain equal hydrostatic  
228 pressures in the device. Confocal images were acquired every 3-5 min for 6 to 8 times to create the

229 entire 3D stack of the gel volume with microvascular formation at each time point. ROIs were selected  
230 considering vascular networks with a clear boundary between vessel wall and gel regions.

231

232 To assess perfusability, fluorescent tracers (FITC-dextran) were introduced through the  
233 microvascular networks by imposing a hydrostatic pressure drop across the gel region between two  
234 medium channels. Videos were recorded using NIS-Elements software (NIKON) on a fluorescent  
235 microscope (Nikon, TI-E ECLIPSE.) at 30 frames per second.

236

### 237 **Quantification of vessel permeability coefficient**

238 The vascular permeability is evaluated as the flux of solute across the walls of the vascular network.  
239 Using mass conservation, the quantity of FITC-dextran crossing the vascular network equals the rate  
240 at which it accumulates outside the vessels in the tissue gel region. According to a previously  
241 described method[40], vascular network permeability,  $P_v$ , was quantified by obtaining the average  
242 intensity of vessels  $I_v$  and tissue (outside vessels)  $I_T$  at two different time points  $t1$  and  $t2$  and using:

$$243 P_v = \frac{1}{(I_v^{t1} - I_T^{t1})} \frac{(I_T^{t2} - I_T^{t1})}{\Delta t} \frac{V}{A_{surface}}$$

244

245 Here,  $\Delta t$  is the time between two images,  $V$  is the tissue volume,  $A_{surface}$  is the surface area of all  
246 vessels in the selected ROI, computed based on the assumption that the ratio  $V/A_{surface}$  can be  
247 estimated as the tissue area  $A_{lateral}$  divided by the perimeter of the vascular region  $L_{branch}$  in the  
248 projected 2D images from the 3D confocal stacks. Diffusion of fluorescent dextran into the gel was  
249 minimized by introducing an iPSC-ECs monolayer in both side channels. The fluorescence intensity  
250 values, vessel surface area and tissue/gel region area were computed using ImageJ.

251

252 **RNA isolation and quantitative RT-PCR**

253 Total RNA was isolated from different conditions using TRIzol reagent (Life Science) for dissolving  
254 fibrin gel. Reverse transcription was performed using SuperScript VILO cDNA synthesis kit  
255 (Invitrogen). Quantitative Real-time RT-PCR (RT-PCR) using SYBR Premix Ex Taq (Takara) or  
256 Power SYBR Green PCR Master Mix, was performed with a 7900HT Fast Real-Time PCR System  
257 (Applied Biosystems). mRNA of endothelial cell adhesion molecule (PECAM-1) also known CD31,  
258 glyceraldehyde 3-phosphate dehydrogenase (GAPDH) and Ribosomal Protein S18 (RPS18) were  
259 used as housekeeping genes, set to 100% as the internal standard. RT-PCR experiments were repeated  
260 at least 3 times for cDNA prepared from 6 devices. Primer sequences (Integrated DNA technology)  
261 are listed in supplementary Table 1. RT-PCR was performed in a scaled up version a of the device  
262 (Supplementary Fig. 1b) in order to collect higher amount of total RNA.

263

264 **Statistical analysis**

265 All data are plotted as mean  $\pm$  SD. One-way ANOVA with pairwise comparisons by the Tukey post  
266 hoc test was used to determine whether three or more data-sets were statistically significant. Statistical  
267 tests were performed using JMP pro (SAS Institutes, Inc.). At least four devices ( $\geq 2$  regions per  
268 device) for each condition within 3 independent experiments were used for the imaging and data  
269 analysis. \*\*\*\* denotes  $p < 0.0001$ , \*\*\* denotes  $p < 0.001$ , \*\* denotes  $p < 0.01$ , \* denotes  $p < 0.05$ .  
270 Non-paired student's t-test was used for significance testing between two conditions.

271

272 **Results**

273

274 **Optimization of self-assembled microvasculature**

275 Three models were established, as described in Methods, with progressively greater complexity: (i)  
276 iPSC-ECs (Fig. 2a,b (i)), (ii) iPSC-ECs + PCs (Fig. 2a,b (ii)), and (iii) iPSC-ECs + PCs + ACs (Fig.  
277 2a,b (iii), Supplementary Figs. 4a-c). In each case, the iPSC-ECs elongated and intracellular  
278 intussusception and vacuoles appeared after 1 day followed by the formation of lumen structures after  
279 2-3 days (Supplementary Figs. 2a and 3a,b). Further development of the  $\mu$ VNs resulted in a highly  
280 interconnected microvasculature by day 7 of the culture (Fig. 2b).

281

282 With iPSC-ECs alone (Fig. 2a,b (i)), vascular networks formed in 4-5 days (Supplementary Fig. 2a),  
283 however, the vessels fused, forming large, elliptical cross-section lumens, many of which contacted  
284 the bottom coverslip (Fig. 3a) and gradually degraded and regressed after 7 days (Supplementary Fig.  
285 5a). In contrast, co-culture of iPSC-ECs with PCs formed smaller and more highly branched vessels  
286 (Figs. 2a,b (ii), 3b). No significant difference could be observed when iPSC-ECs were cultured alone  
287 or with PC conditioned medium (Supplementary Fig. 5b), suggesting that contact with PCs effectively  
288 facilitated endothelial organization, by stabilizing a mature vasculature with a morphology more  
289 similar to that found *in vivo*.

290

291 The addition of ACs further assisted in the development of a complex inter-connected and branched  
292 architecture found in native vasculatures (Fig. 2a,b (iii), Supplementary Fig. 3a,b). In tri-culture with  
293 ACs, the  $\mu$ VNs exhibited distinctive behavior during formation, with increased tortuosity and vessels  
294 extending higher up in the 3D gel (Fig. 3c). A fundamental characteristic of the BBB is the stratified  
295 organization of cells around the vessels and their direct contact interactions. In 4 replicates with 10-  
296 12 high resolution confocal images, we observed a spontaneous self-organization into multicellular  
297 BBB structures. Indeed, PCs (F-actin, red, Fig. 2c) adhered to both sides of the endothelial cell

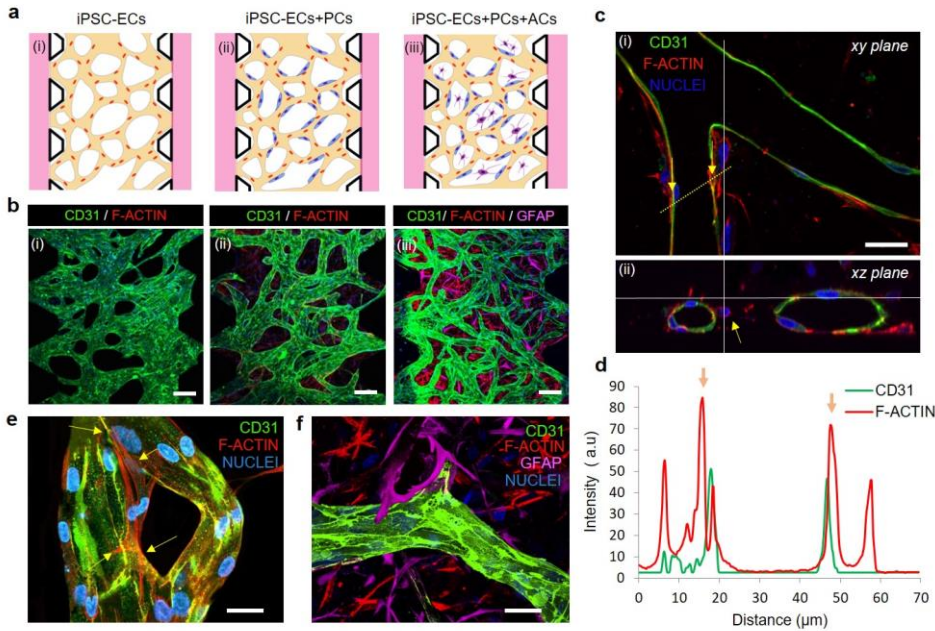
**Commentato [CM1]:** If reviewer would like to specify how many biological replicates/highly resolution confocal, numbers are more than 4 replicates with 10-12 images.

298 surface, surrounding the vessel (CD31, green, Fig. 2c,e, Supplementary Fig. 6a, Supplementary video  
299 1). For example, tracing the intensity profiles of EC and PC fluorescence (Fig. 2d), F-actin expression  
300 was observed outside the vessel, clearly delineating the presence of PCs. These results showed that  
301 pericytes partially overlapped the outer surface of the EC layer exhibiting a BBB-like organization.  
302 In addition, 3D rendering of vessel bifurcations showed PCs in contact with the endothelium at  
303 multiple locations (Fig. 2e). Moreover, direct physical contacts were observed between AC endfeet  
304 (Glial Fibrillary Acidic Protein, (GFAP), violet) and the abluminal surface of the brain vessels (CD31,  
305 green, Fig. 2f; Supplementary Figs. 6b,c).

306

### 307 **Characterization of microvascular parameters**

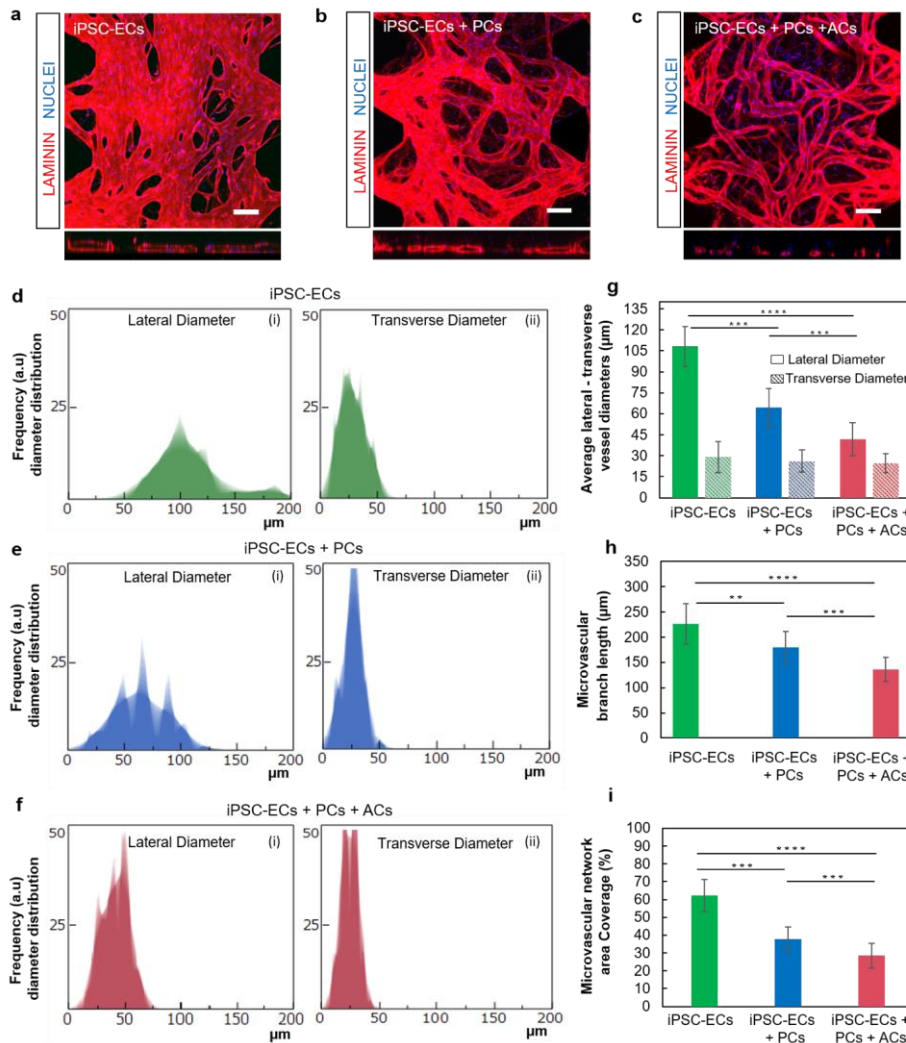
308 To determine the geometrical changes in the  $\mu$ VNs (Fig. 3a-c, Supplementary Fig.4a-c), lateral and  
309 transverse vessel diameter distributions, percentage of image area containing vascular networks, and  
310 total branch length were each quantified (Fig. 3d-i). As expected, in the iPSC-ECs+PCs co-culture,  
311 the lateral vessel diameters (30 to 100  $\mu$ m, Fig. 3e (i)) were significantly lower than in mono-culture  
312 conditions (50 to 150  $\mu$ m with a few outliers to 200  $\mu$ m, Fig. 3d (i)). Lateral diameters were further  
313 reduced by adding ACs (most values between 25 and 50  $\mu$ m (Fig. 3f (i))). The overall transverse  
314 diameter distributions were similar for all three conditions, ranging between 10 and 40  $\mu$ m, and  
315 centered around 30  $\mu$ m (Fig. 3d-f (ii)).



316

317 **Figure 2: Microvascular network conditions iPSC-ECs - PCs/ACs contact interactions.** (a)  
 318 Schematic representation and (b) confocal images of (a, b, (i)) iPSC-ECs mono-culture (CD31,  
 319 green), (a, b, (ii)) co-culture with PCs (F-actin, red), and (a, b, (iii)) tri-culture with PCs and ACs  
 320 (GFAP, magenta), after 7 days of culture in the microfluidic device. (c) Cross-sectional images of  
 321 blood microvessels showing hollow lumens. (c, (i)) PCs adhered to and partially enveloped brain  
 322 microvessel. (c, (ii)) Cross-sectional images of blood microvessels showing a lumen enclosed by  
 323 iPSC-ECs and PCs. PCs surround the blood vessel. Image shows how section was sampled using a  
 324 line scan measurement (yellow line) and generation of intensity profile histogram. (d) Intensity  
 325 profile analysis of CD31/F-actin in iPSC-ECs -PCs interaction corresponding to the yellow line scan.  
 326 Intensity profile shows distinct peaks (yellow arrow) at the position of contact interaction/overlapping  
 327 between ECs and PCs. CD31 expression (green) was low when F-actin expression (red) was high,  
 328 further indicating that F-actin expression belonged only to brain PCs outside the vessels. Region of  
 329 low green intensity corresponds to the vascular bed of the vessel. (e) Contact interactions of PCs  
 330 enveloping blood microvessel. PCs adhered to and partially enveloped brain microvessel. (f)  
 331 Confocal image of iPSC-ECs, PCs and ACs in the tri-culture condition. Images were analyzed using  
 332 Imaris 8.3. Scale bars indicate 100  $\mu\text{m}$  (b) and 20  $\mu\text{m}$  (c, e, f).

333



334

335 **Figure 3: 3D BBB microvascular network parameter quantification.** Confocal images of laminin  
 336 expression (red) and nuclei (DAPI, blue) of 3D BBB  $\mu$ VN maturation from (a) mono-culture of iPSC-  
 337 ECs, (b) co-culture of iPSC-ECs+PCs and (c) tri-culture of iPSC-ECs+PCs+ACs (scale bar: 100  $\mu$ m).  
 338 Distribution of lateral and transverse vessel diameter measurements of 3D BBB  $\mu$ VNs formed by  
 339 vasculogenesis, for (d) mono-culture of iPSC-ECs, (e) co-culture with brain PCs, (f) tri-culture with  
 340 brain PCs and ACs. Additional image in supplementary Fig. 4. (g, h, i) Quantification of  
 341 microvascular network parameters: (g) average lateral and transverse vessel diameters in each  
 342 condition, (h) microvascular branches average length and (i) percentage ratio of microvascular  
 343 network area coverage to the total area. \*  $p < 0.05$ , \*\*  $p < 0.01$ , \*\*\*  $p < 0.001$ , \*\*\*\*  $p < 0.0001$ . Error bars  
 344  $\pm$  SD,  $n = 30$ .

345 Hence, lumens with nearly circular cross-section and consequently smaller cross-section area and  
346 higher circularity (Supplementary Fig. 6d-f) formed in the tri-culture condition (average lateral  
347 diameter:  $42 \pm 13 \mu\text{m}$ , average transverse diameter:  $25 \pm 6 \mu\text{m}$ , Fig. 3g), while lumens were flattened  
348 and had elliptical cross-section in mono-cultures (average lateral diameter:  $108 \pm 14 \mu\text{m}$ , average  
349 transverse diameter:  $29 \pm 10 \mu\text{m}$ , Fig. 3g), and in co-cultures (average lateral diameter:  $64 \pm 13 \mu\text{m}$ ,  
350 average transverse diameter:  $27 \pm 7 \mu\text{m}$ , Fig. 3g).

351

352 Moreover, the cumulative average  $\mu\text{VN}$  **branch** length decreased from mono-culture ( $226 \pm 40 \mu\text{m}$ ),  
353 to co-culture ( $179 \pm 31 \mu\text{m}$ ), and tri-culture ( $136 \pm 24 \mu\text{m}$ ) conditions, respectively (Fig. 3h),  
354 demonstrating a highly complex and intertwined vascular network. Accordingly, the networks with  
355 iPSC-ECs, iPSC-ECs+PCs, and iPSC-ECs+PCs+ACs conditions covered progressively less area in  
356 the projected image (62%, 42%, and 28%, respectively (Fig. 3i). Indeed, in tri-culture conditions, the  
357  $\mu\text{VNs}$  showed improved morphology provided by the co-culture with ACs and PCs, with reduced  
358 vessel diameters and average branch length. These results mirror similar observations that have been  
359 attributed to the secretion of angiogenic growth factors by PCs and ACs [19][20].

360

361 In summary, these results indicate that the networks formed with all three cell types --iPSC-  
362 ECs+PCs+ACs -- contained more stable and shorter vessel branches, with more circular cross-  
363 sections and smaller vessel diameters compared to the other conditions. These networks also  
364 exhibited more random interconnections and improved 3D structural orientation into the gel region:  
365 such structure is more similar to *in vivo* vessel morphology [30].

366

### 367 **Protein synthesis and gene expression related to blood-brain barrier (BBB)**

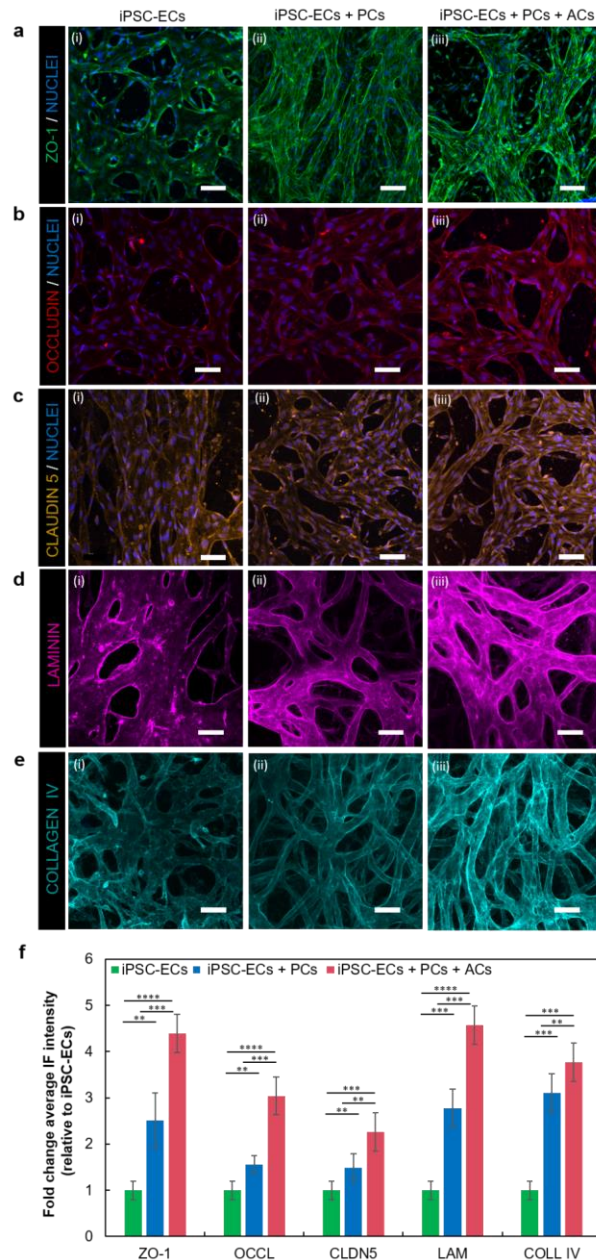
368 To analyze whether the engineered 3D brain microvascular model constitutes a functional barrier and  
369 exhibits physiological characteristics typical of the BBB present *in vivo*, we validated and compared

370 protein expression measured by immunocytochemistry assays and quantitative real-time RT-PCR,  
371 performed after 7 days. Firstly, immunocytochemistry images of vascular networks obtained under  
372 different culture conditions were compared from multiple regions of interest (ROIs) within the  
373 vessels. The expression of endothelial-specific junction proteins ZO-1, occludin, and claudin-5 (Fig.  
374 4a-c), and ECM constituents such as laminin (Fig. 4d) and collagen IV (Fig. 4e) was analyzed by  
375 confocal microscopy (See also Supplementary fig. 7b-f). Interestingly, the increase of TJ protein  
376 expression in  $\mu$ VNs was observed by introducing PCs and ACs (Fig. 4a-c). Therefore, the BBB  $\mu$ VNs  
377 obtained by iPSC-ECs+PCs+ACs tri-culture (Fig. 4a (iii)) relatively expressed much higher level of  
378 ZO-1, occludin and claudin-5 compared to mono-culture of iPSC-ECs and iPSC-ECs+PCs (Fig. 4a-  
379 c). Quantitative analysis of fold change average immunofluorescent (IF) intensity (relative to iPSC-  
380 ECs) confirmed qualitative observations (Fig. 4f). Average immunofluorescent (IF) intensity was  
381 calculated by dividing the total immunofluorescent intensity by the cell boundary length in each ROI  
382 in the case of tight-junction proteins (ZO-1, occludin, and claudin-5). In the case of basement  
383 membrane protein deposition (laminin, collagen IV), average IF intensity was calculated by dividing  
384 the total IF intensity by the vascularized area in each ROI. ROIs were selected to contain only  
385 microvascular portions (Fig. 4f). Continuous cell-cell junctions lining the rhomboidal boundaries of  
386 endothelial cells along lumens were observed in co-culture and tri-culture conditions, as demonstrated  
387 by the clear delineation of ZO-1 along the cell-cell border (Supplementary Fig. 7a).

388

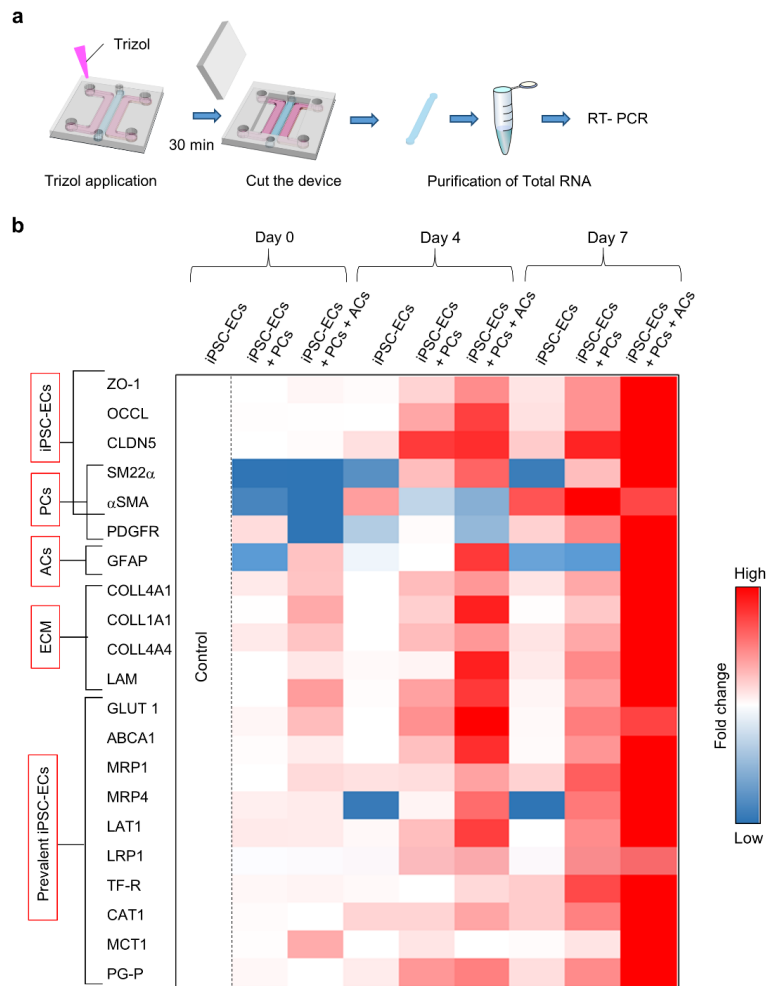
389 Another sign of vessel maturation was the deposition of basement membrane proteins, exhibiting a  
390 similar trend to TJ expression. Laminin and collagen IV immunofluorescence intensity (Fig. 4d-f)  
391 approximately doubled in the case of the microvascular networks obtained by iPSC-ECs+PCs+ACs  
392 tri-culture (Fig. 4d,e (iii)) compared to iPSC-ECs mono-culture (Fig. 4d,e (i)) and was significantly  
393 higher than for iPSC-ECs+PCs co-culture (Fig. 4d,e (ii)).

394 **Figure 4: Immunocytochemistry**  
 395 **analysis of tight junctions and**  
 396 **ECM deposition.** Self-assembled  
 397 microvascular networks formed  
 398 after 7 days in microfluidic device  
 399 culture for: (i) mono-culture of  
 400 iPSC-ECs, (ii) co-culture with PCs  
 401 and (iii) tri-culture with PCs and  
 402 ACs (BBB microvascular network  
 403 model). (a-e) Microvascular  
 404 networks were immunostained for  
 405 tight junctions (ZO-1, occludin  
 406 (OCCL) and claudin-5 (CLDN 5)),  
 407 and ECM production (laminin  
 408 (LAM) and collagen IV (COLL  
 409 IV)), and nuclei (DAPI) inside  
 410 microfluidic devices and imaged by  
 411 confocal microscopy. (a)  
 412 Immunofluorescent (IF) intensities  
 413 of ZO-1 were well-defined in co-  
 414 culture and tri-culture conditions.  
 415 ZO-1 expression was clearly  
 416 localized at the intersection between  
 417 cells forming a rhomboidal grid,  
 418 characteristic of mature and well-  
 419 organized microvasculature.  
 420 Instead, monoculture exhibited low  
 421 expression of TJ proteins with no  
 422 visible and defined accumulation at  
 423 cell boundaries. Similar behavior  
 424 was exhibited by (b) occludin and  
 425 (c) claudin-5. (d) Confocal images  
 426 of deposition of laminin and (e)  
 427 collagen IV showed production and  
 428 remodelling of a distinct ECM by  
 429 the different microvascular  
 430 networks. BBB microvascular  
 431 model with PCs and ACs expressed  
 432 higher intensities of laminin and  
 433 collagen IV compared to  
 434 monoculture and co-culture,  
 435 providing evidence that PCs and  
 436 ACs improved vascular function.  
 437 Qualitative image tests were  
 438 realized by ROI intensity analysis. (f)  
 439 Fold change average IF intensity (relative to iPSC-ECs)  
 440 quantify the protein expression according to the IF images. Computed image intensities were  
 441 normalized by the selected area. \*  $p < 0.05$ , \*\*  $p < 0.01$ , \*\*\*  $p < 0.001$ , \*\*\*\*  $p < 0.0001$ . Error bars  $\pm$  SD,  
 442  $n = 8$ . Confocal image scale bar: 50  $\mu\text{m}$ .



442 To confirm immunocytochemistry results, total RNA was extracted from the total cell population in  
443 the microfluidic device (Fig. 5a) and purified from different conditions at several time points (day 0,  
444 4, and 7). RT-PCR analysis was conducted considering gene markers of TJ proteins, ECM production  
445 and several endothelial membrane transporters such as efflux-pumps, passive transports, solute  
446 carriers, and receptor-mediated mechanisms. Vessel maturation was investigated in terms of the  
447 expression of several markers and proteins, in the case of co-culture and tri-culture conditions, and  
448 was compared to the control condition (iPSC-ECs). The mRNA expression of each gene was  
449 measured relative to the expression of CD31 and GAPDH (fold change). TJ proteins such as ZO-1,  
450 occludin, and claudin-5 were highly up-regulated in the tri-culture condition at day 7 compared to  
451 mono-culture and co-culture conditions. Interestingly, the expression of TJ markers in the tri-culture  
452 case increased as a function of culture time (Fig. 5b, Supplementary Fig. 10a-e). As expected, GFAP  
453 was regulated exclusively in the presence of ACs. PDGFR gene expression was slightly higher in the  
454 tri-culture condition while alpha-smooth muscle actin ( $\alpha$ SMA) expression was reduced, possibly due  
455 to the increased proliferation of iPSC-ECs and PCs stimulated by ACs. Furthermore, basement  
456 membrane proteins (collagen IV, laminin) were highly expressed over time in the tri-culture condition  
457 compared to the mono- and co-culture cases. In addition, gene expression of several BBB-specific  
458 membrane transporters and receptors which exploit several transport mechanisms (passive diffusion,  
459 ATP-binding efflux transporter, solute carriers and receptor-mediated transcytosis), such as P-GP,  
460 MRP1, MRP4, TF-R, LRP1, LAT-1, GLUT-1, CAT1, MCT1, ABCA1, and BCRP widely increased  
461 over time in the tri-culture BBB model (iPSC-ECs+PCs+ACs), compared to iPSC-ECs+PCs and  
462 iPSC-ECs microvascular network conditions. Overall after 7 days, the tri-culture condition displayed  
463 a constantly increased maturation and upregulation of all examined genes (Fig. 5b, Supplementary  
464 Fig. 10a-e, Primer sequences in Supplementary Table 1).

465

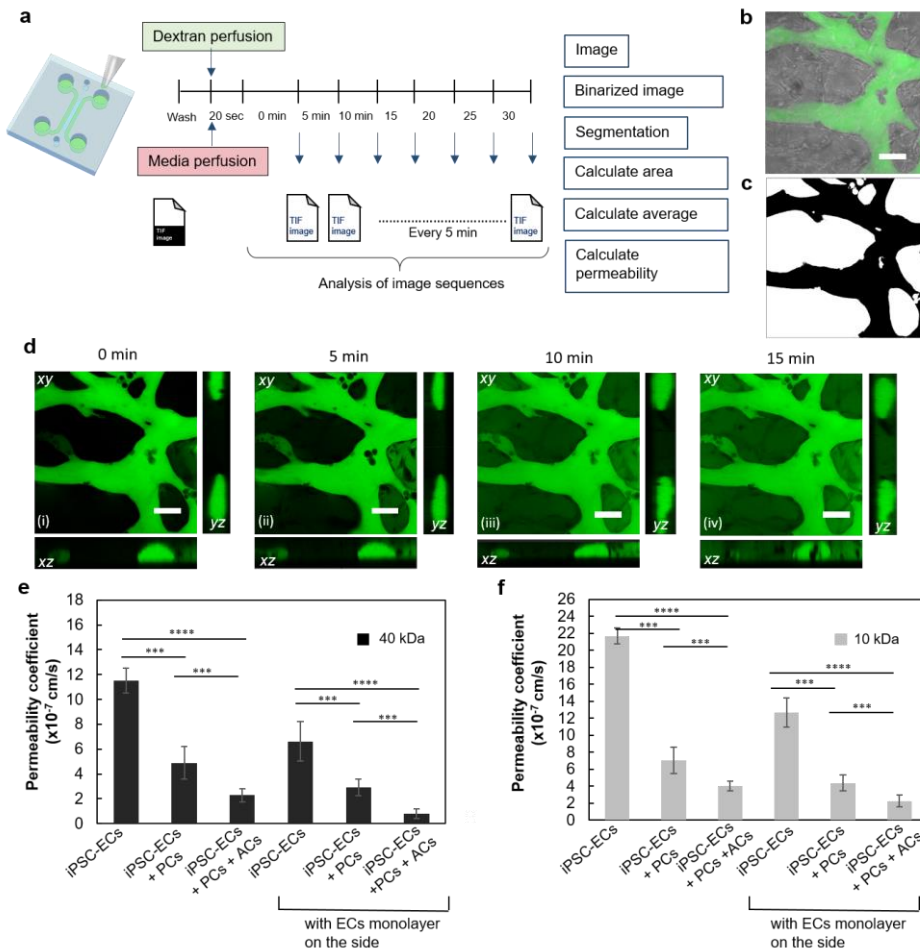


466 **Figure 5: Quantitative relative RT-PCR of 3D BBB  $\mu$ VNs in microfluidic device.** (a) Schematic  
 467 representation of vascular network and gel extraction from a microfluidic device, purification of total  
 468 RNA and conduct of RT-PCR experiments. (b) Heatmap of RT-PCR results of mono-culture of iPSC-  
 469 ECs, co-culture with PCs, and tri-culture with PCs and ACs at 0, 4 and 7 days. Relative comparison  
 470 of mRNA expression of factors relating to microvascular maturation and other typical BBB features.  
 471 Gene analysis considered markers 1) expressed in ECs, 2) expressed in PCs, 3) expressed in ACs, 4)  
 472 ECM protein RNA, and 5) genes expressed predominantly by ECs, but also in smaller amounts by  
 473 the other two cell types. Fold change was relative to control (mono-culture of iPSC-ECs, day 0). The  
 474 internal standard housekeeping gene was CD31.  $0.01 < p < 0.05$ ,  $n = 3$ .

475 **Distinct cell contributions to BBB permeability**

476 The permeability of the microvessels in our BBB  $\mu$ VN models was computed to assess the practical  
477 potential to use our system to mimic solute transport *in vivo*. In all culture conditions, vessels  
478 comprising the entire vascular network were well formed and completely perfusable at day 7  
479 (Supplementary Fig. 8d, Supplementary video 2, 3). Permeability coefficients were measured by  
480 introducing solutions containing FITC-dextran tracers in the vasculature (10 & 40 kDa), and  
481 capturing confocal images at 5 min intervals and computing them as explained in Methods (Fig.  
482 6a-d, Supplementary Fig. a-c). With side-channels seeded with iPSC-ECs, permeability to 40 kDa  
483 FITC-dextran of the  $\mu$ VN obtained under mono-, co-, and tri-culture conditions progressively  
484 decreased: 6.6, 2.5, and  $0.89 \times 10^{-7}$  cm/s, respectively. A similar trend was observed for the 10 kDa  
485 FITC-dextran: 12, 4.8 and  $2.2 \times 10^{-7}$  cm/s, respectively (Fig. 6e, f). When iPSC-ECs were not added  
486 to the side channels, leakage of tracer across the side-walls of the gel region gave rise to higher  
487 permeability values, roughly a two-fold increase, due to the artifact associated with the additional  
488 source of tracer influx. Side channel seeding helped in several ways. It improved coverage of the  
489 exposed side gel surface with an endothelial monolayer, filled gaps that sometimes formed at the gel-  
490 post borders, and increased the number and patency of connections between the networks and the  
491 main channel (Fig. 7a and Supplementary Fig. 9a-e).

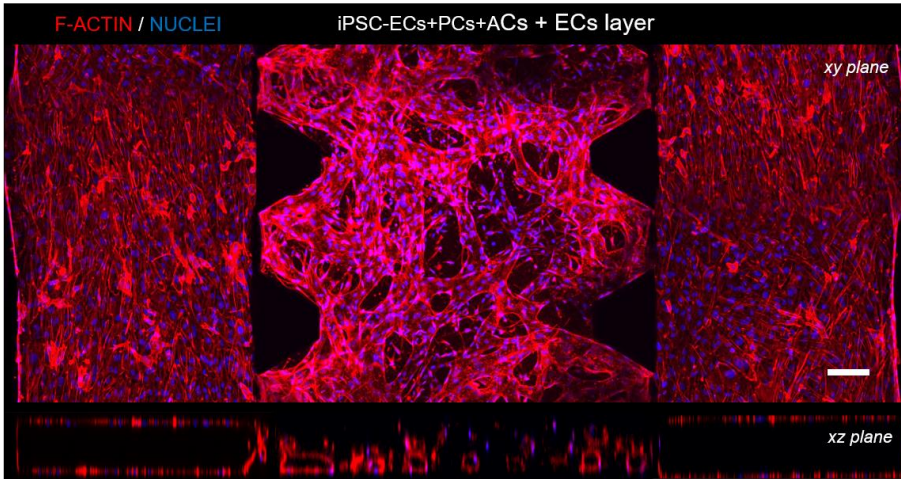
492



493

494 **Figure 6: Permeability assay in BBB model.** (a) Timeline of permeability experiments and  
 495 computational analysis. After cell culture medium was removed, dextran solution was injected and  
 496 image stacks were captured every 3-5 mins for 30 mins. Workflow of image analysis by ImageJ and  
 497 permeability coefficient calculation. (b) Confocal and bright field images at time 0. (c) Image  
 498 binarization after thresholding to identify vessel borders. (d, (i-iv)) Maximum image projections and  
 499 cross-sections including xy, xz and yz planes at 4 time-points. The graphs show permeability  
 500 coefficients for 3 different conditions (with and without ECs seeding in side channels) using (e) 40  
 501 kDa and (f) 10 kDa FTIC-dextran in mono-culture of iPSC-ECs, co-culture of iPSC-ECs+PCs, and  
 502 tri-culture of iPSC-ECs+PCs+ACs. The data show mean value, error bars  $\pm$  SD,  $n=10$ , \*  $p<0.05$ , \*\*  
 503  $p<0.01$ , \*\*\*  $p<0.001$ , \*\*\*\*  $p<0.0001$ , scale bars 50  $\mu$ m.

a



504

505 **Figure 7: BBB microvascular network model.** (a) Confocal images of xy and xz (cross-section)  
506 planes of the 3D BBB microvascular *in vitro* model with iPSC-ECs+PCs+ACs, including EC layers  
507 in the side channel. Scale bars 200  $\mu\text{m}$ .

## 508 **Discussion**

509

510 In this work, we developed a new *in vitro* human BBB microvascular model consisting of a self-  
511 assembled  $\mu$ VN of iPSC-ECs co-cultured with brain PCs and ACs. Novelty of our microfluidic  
512 platform arises from simultaneous seeding of three human cell types into a single gel region,  
513 producing a perfusable vascular network, with permeabilities lower than those of other published  
514 microfluidic models [23][24][27][32][34].

515

516 iPSC-ECs were selected as they are immature endothelial cells, capable of organizing into a complex  
517 and perfusable vascular network [41], with lower permeability values compared to other non-brain  
518 EC models [42][43][44]. The potential features of iPSC-ECs may contribute to a coherent and  
519 relevant replacement of “brain” endothelial cells to establish a 3D BBB microvascular model.  
520 Moreover, iPSC cells may be potentially derived from patients who suffer from specific  
521 neurodegenerative diseases [45], thereby producing a pathological model to study disease progression,  
522 to screen for drugs appropriate for patients’ sub-groups, or even for precision medicine applications  
523 to select optimal, personalized therapies.

524

525 Our 3D BBB  $\mu$ VN model incorporating three cell-types (Fig. 1b and Fig. 7a) expressed both  
526 functional and morphological characteristics present in the human BBB, with stable and perfusable  
527  $\mu$ VNs, comprising small lumens with circular cross-section comparable with *in vivo* human  
528 microcirculation (arterioles and venules  $<100\ \mu\text{m}$ ; capillaries  $<10\ \mu\text{m}$ ) [28][29]. It also defined  
529 microvascular branch length similar to segments in close proximity to the third ventricle (caudate,  
530 putamen, and thalamus with an average of  $70\ \mu\text{m}$ ) [46] and characterized by low permeability and  
531 transport selectivity (Fig. 6e,f and Supplementary movie 2, 3). It draws upon the intrinsic nature of  
532 ECs interacting with other neural cell types to recapitulate brain vascular morphogenesis during  
533 developmental process via vasculogenesis [47][48], in which immature ECs recruit PCs and ACs to

534 form new vessels through PDGFR and Sonic hedgehog (SHH) signaling pathways [47][49]. In  
535 particular, PCs played an important role to create a robust and stable vessel network with significant  
536 lateral diameter reduction (Fig. 3d,g). It has been previously demonstrated that ECs need a  
537 combination of juxtacrine and paracrine signaling to create a stable and physiologically-relevant  
538 microvasculature on a chip [38][39]. Hence, the resulting formation of a physiologically-relevant  
539 microvasculature, was facilitated by juxtacrine interactions and paracrine signaling between iPSC-  
540 ECs and PCs (enveloping the endothelium) (Fig. 2c-e), along with the increase of TJ expression and  
541 appropriate concentration of growth factors (Fig. 4a-c, Supplementary Figs. 7a-d, 10a-d). Indeed,  
542 improvements were associated with the presence and secretion of vascular endothelial growth factor  
543 VEGF (50 ng/ml in the supplemented medium), angiopoietin-1 (ANG-1) and fibroblast growth factor  
544 (FGF) by stromal cells, especially PCs [50]. However, as VEGF could modulate vascular  
545 permeability through the disruption of tight junctions and consequent break down of the BBB [51],  
546 cell culture medium was supplemented with VEGF up to day 4.

547

548 We hypothesize that this morphological change in the final structure of the BBB  $\mu$ VNs was induced  
549 by not only the presence and cell-secretion of pro-angiogenic and vasculogenic growth factors and  
550 ECM proteins, but also by juxtacrine signaling, consistent with previous findings [35][52][53]. Our  
551 results also suggest that PCs not only influence the creation of vascular networks but also induce the  
552 differentiation of iPSC-ECs into brain-specific endothelial cells, as determined by the RT-PCR results  
553 (Fig. 5b, Supplementary Fig. 10a-d). Indeed, it has already been shown that co-culture of ECs with  
554 PCs is required for BBB formation and the maintenance of homeostasis by contact and paracrine  
555 interactions [54].

556

557 In addition to the contribution of PCs, ACs also improved BBB formation and integrity. iPSC-ECs  
558 self-assembled into mature vascular networks forming complex structures when interacting with both  
559 cell types. The role of ACs was evidenced by an increase in the expression of BBB transporters and

560 TJ proteins, such as ZO-1, occludin, claudin-5, ECM deposition (Figs. 4a-e, 5b, Supplementary Fig.  
561 7a-c), and the corresponding decrease in permeability, (Fig. 6e-f) similar to previous transwell and  
562 microfluidic-based models incorporating ACs [55]. In particular, the upregulation of typical BBB  
563 transporters such GLUT-1, LAT-1, PG-P, TF-R, LRP1 and MRPs is fundamental to obtain an *in vitro*  
564 BBB model for drug design and testing. Indeed, these specific transporters were highlighted as  
565 potential targets to enhance the penetration of drugs into the brain [56] (Supplementary Fig. 10d).

566

567 In our model, AC endfeet were directly attached to the surface of vascular networks in the 3D matrix  
568 (Fig. 2f, Supplementary Fig. 6b,c). This morphological feature of ACs recapitulates their  
569 physiological arrangement in the brain and provides mutual biochemical support for those cells,  
570 helping to maintain the integrity of the neurovascular networks [57]. Our findings suggest that the  
571 addition of ACs is in part responsible for the improved morphology of BBB anatomical structure.  
572 They might also contribute through paracrine signals to the development of a BBB-like endothelial  
573 phenotype since ACs are known to regulate influx/efflux, vasodilatation/vasoconstriction by inducing  
574 tightening of the endothelium [19], as well as cytokine and growth factor secretion such as basic FGF,  
575 glial-derived neurotrophic factor (GDNF), and ANG-1 [58]. Further investigation is needed to  
576 ascertain the relative importance of different biological pathways and factors improving BBB  
577 integrity, however, direct adhesion of ECs, PCs and ACs might facilitate N-cadherin cell-cell  
578 interactions [47].

579

580 As key features in assessing the value of BBB microvascular models for drug transport studies,  
581 vascular perfusability and permeability were measured using fluorescent probes. The vessel networks  
582 in our tri-culture BBB model attained permeability values of  $8.9 \times 10^{-8}$  cm/s and  $2.2 \times 10^{-7}$  cm/s for 40  
583 kDa and 10 kDa FTIC-dextran, respectively (Fig. 6e,f), confirming barrier selectivity depending on  
584 their molecular weight [59].

585 Importantly, these values are comparable to those measured *in vivo* in rat cerebral microcirculation

586 (3.1 ± 1.3×10<sup>-7</sup> cm/s for a 10 kDa FITC-dextran) [60], (1.37± 0.26×10<sup>-7</sup> cm/s for a 40 kDa FITC-  
587 dextran) [61], and similar to specific models that employ brain ECs derived from iPSCs (IMR90-4)  
588 by co-culturing with astrocytes and/or neurons [62][63], and lower than previously reported 3D  
589 [23][27][32][34], or 2D BBB models [24][64].

590

591 As a side note, inclusion of an iPSC-EC monolayer in the adjacent fluidic channels improved vascular  
592 perfusability and also reduced the artifacts associated with tracer leakage across the sidewalls of the  
593 gel region (Fig. 7, Supplementary Fig. 9a-e). Consistent with the progressive reduction in  
594 permeability with increasing model complexity, we observed a corresponding increase in the tightness  
595 of junctional proteins and their regulation [53][65], evaluated by immunostaining and RT-PCR  
596 analysis. This contrasts with a previous study that reported an increase in permeability coefficient  
597 when human brain endothelial cells (hCMEC/d3) were co-cultured with ACs isolated from rats [32],  
598 possibly due to cross-species effects, as suggested by the authors of [29].

599

600 It is important to note that our model lacked neurons and microglia, and these might have further  
601 effects on barrier functionality. Recent literature has shown that the upregulation of BBB-specific  
602 transporters and the differentiation of brain-specific ECs are induced by the co-culture of iPSC-ECs  
603 with iPS derived neurons [66]. In the same model authors demonstrated the possibility of drug  
604 screening using iPSC-ECs in combination with all human iPS derived cells using transwell methods.  
605 Also, co-culture with neural iPSCs has been found to improve EC barrier integrity and decrease  
606 vascular permeability [66]. Therefore, there appear to be additional advantages gained by an even  
607 more comprehensive human patient-derived *in vitro* model [66], combining iPSCs and/or neural stem  
608 cells with the vascular networks, PCs, and ACs described here. Moreover, using iPS cells derived  
609 from patients affected by neurological disorders [45], such as Alzheimer's disease, a BBB  
610 pathological model could be obtained.

611

612 Our 3D self-organized system has several advantages compared to the *in vitro* 2D membrane-based  
613 monolayer, including its more physiologically-relevant morphology. Permeability measurements,  
614 however, at this point are limited to quantifying concentrations of a fluorescent tracer. Similar  
615 measurements could be made by tagging the molecule of interest with a fluorescent marker using this  
616 same experimental protocol. Alternatively, samples of interstitial fluid could be directly collected  
617 from the gel filling ports in the device, and used to quantify transport into the matrix, but this could  
618 be problematic due to the low drug concentrations in the gel region.

619 Although PDMS is widely used for microfluidic applications, one of its disadvantages is non-specific  
620 adsorption of proteins and small hydrophobic molecules during long-term interaction [67]. Even  
621 though this would not have affected our current permeability study, in perspective of drug testing,  
622 several treatments exist to prevent fouling of the PDMS surface. Accordingly, distinct surface  
623 modifications that could reduce non-specific absorption include coating the PDMS surface with  
624 bovine serum albumin (BSA) [68], grafting with anti-fouling molecules [69], or silanization [70].

625

626 Other possible improvements to the current model are the introduction of continuous perfusion to  
627 improve microvascular formation and reduce vascular permeability in the perspective of a long-term  
628 culture system. Indeed, flow perfusion culture could advance the model in two important aspects.  
629 Firstly, oxygen and glucose transport into the vessels will tend to modulate glycolytic metabolism in  
630 favor of the more efficient aerobic respiration useful for maintaining a long-term culture. Secondly,  
631 flow-mediated shear stress is known to promote the differentiation of vascular endothelial cells into  
632 a more BBB-like phenotype with the highest expression of TJ proteins and membrane transporters,  
633 producing further reductions in permeability [71]. Finally, it would be beneficial to assess the trans-  
634 endothelial electrical resistance (TEER) measurement as another metric of BBB function [24].

635

636 **Conclusion**

637

638 Here we present the first highly functional 3D BBB *in vitro* model produced by vasculogenesis that  
639 incorporate human iPSC-ECs microvascular network in contact interaction with human brain PCs  
640 and ACs within a single 3D ECM/fibrin gel region. Our 3D BBB microvascular model exhibits  
641 physiologically relevant structures and provides an effective and reproducible platform compared to  
642 static models [16][17], useful in the study of dynamic transport of small and large molecules across  
643 the BBB in a complex microenvironment [72]. We believe this is a reliable and valuable next-  
644 generation system that furthers the understanding of neurovascular function, enables the preclinical  
645 development of effective CNS therapeutics [16], can be applied to probe metastatic cancer  
646 extravasation [26][73] and evaluate reciprocal brain-systemic circulation interactions that occur in  
647 inflammatory and neurodegenerative diseases [4-9]. This translational model could be adapted for the  
648 high-throughput pre-clinical screening of innovative therapies targeting specific BBB transporters, to  
649 perform drug delivery studies and to investigate the transport of microengineered nanocarriers able  
650 to cross the BBB.

651 **References**

652

- 653 [1] N. J. Abbott, "Dynamics of CNS barriers: Evolution, differentiation, and modulation," *Cell. Mol.*  
654 *Neurobiol.*, vol. 25, no. 1, pp. 5–23, 2005.
- 655 [2] N. J. Abbott, A. A. K. Patabendige, D. E. M. Dolman, S. R. Yusof, and D. J. Begley, "Structure and  
656 function of the blood-brain barrier," *Neurobiol. Dis.*, vol. 37, no. 1, pp. 13–25, 2010.
- 657 [3] Y. Serlin, I. Shelef, B. Knyazer, and A. Friedman, "Anatomy and physiology of the blood-brain  
658 barrier," *Semin. Cell Dev. Biol.*, vol. 38, pp. 2–6, 2015.
- 659 [4] R. D. B. V. Zlokovic, "Neurovascular mechanisms and blood–brain barrier disorder in  
660 Alzheimer’s disease," *Acta Neuropathol.*, vol. 36, no. 3, pp. 490–499, 2010.
- 661 [5] B. V. Zlokovic, "Neurovascular mechanisms of Alzheimer’s neurodegeneration," *Trends Neurosci.*,  
662 vol. 28, no. 4, pp. 202–208, 2005.
- 663 [6] R. Kortekaas *et al.*, "Blood-brain barrier dysfunction in Parkinsonian midbrain *in vivo*," *Ann. Neurol.*,  
664 vol. 57, no. 2, pp. 176–179, 2005.
- 665 [7] E. Waubant, "Biomarkers indicative of blood-brain barrier disruption in multiple sclerosis.," *Dis.*  
666 *Markers*, vol. 22, no. 4, pp. 235–244, 2006.
- 667 [8] R. K. Jain, E. Di Tomaso, D. G. Duda, J. S. Loeffler, A. G. Sorensen, and T. T. Batchelor,  
668 "Angiogenesis in brain tumours," *Nat. Rev. Neurosci.*, vol. 8, no. 8, pp. 610–622, 2007.
- 669 [9] B. T. Hawkins and T. P. Davis, "The Blood-Brain Barrier / Neurovascular Unit in Health and  
670 Disease," *Pharmacol. Rev.*, vol. 57, no. 2, pp. 173–185, 2005.
- 671 [10] W. M. Pardridge, "CSF, blood-brain barrier, and brain drug delivery.," *Expert Opin. Drug Deliv.*, vol.  
672 5247, no. May, pp. 1–13, 2016.
- 673 [11] W. M. Pardridge, "Why is the global CNS pharmaceutical market so under-penetrated?," *Drug*  
674 *Discov. Today*, vol. 7, no. 1, pp. 5–7, 2002.
- 675 [12] W. M. Pardridge, "Blood-brain barrier drug targeting: the future of brain drug development.," *Mol.*  
676 *Interv.*, vol. 3, no. 2, pp. 90–105, 51, 2003.
- 677 [13] N. J. Abbott, "Prediction of blood–brain barrier permeation in drug discovery from *in vivo*, *in vitro*  
678 and *in silico* models," *Drug Discov. Today Technol.*, vol. 1, no. 4, pp. 407–416, Dec. 2004.
- 679 [14] D. Pamies, T. Hartung, and H. T. Hogberg, "Biological and medical applications of a brain-on-a-  
680 chip.," *Exp. Biol. Med. (Maywood)*, pp. 1096–1107, 2014.
- 681 [15] P. S., "Preclinical research: Make mouse studies work," *Nature*, vol. 507, no. 425, 2014.
- 682 [16] R. Cecchelli *et al.*, "Modelling of the blood–brain barrier in drug discovery and development," *Nat.*  
683 *Rev. Drug Discov.*, vol. 6, no. 8, pp. 650–661, 2007.
- 684 [17] M. W. van der Helm, A. D. van der Meer, J. C. T. Eijkel, A. van den Berg, and L. I. Segerink,  
685 "Microfluidic organ-on-chip technology for blood-brain barrier research.," *Tissue barriers*, vol. 4, no.  
686 1, p. e1142493, 2016.

- 687 [18] K. Hatherell, P. O. Couraud, I. A. Romero, B. Weksler, and G. J. Pilkington, "Development of a  
688 three-dimensional, all-human in vitro model of the blood-brain barrier using mono-, co-, and tri-  
689 cultivation Transwell models," *J. Neurosci. Methods*, vol. 199, no. 2, pp. 223–229, 2011.
- 690 [19] N. J. Abbott, L. Rönnbäck, and E. Hansson, "Astrocyte-endothelial interactions at the blood-brain  
691 barrier," *Nat. Rev. Neurosci.*, vol. 7, no. 1, pp. 41–53, 2006.
- 692 [20] M. D. Sweeney, S. Ayyadurai, and B. V. Zlokovic, "Pericytes of the neurovascular unit: key functions  
693 and signaling pathways," *Nat. Neurosci.*, vol. 19, no. 6, pp. 771–783, 2016.
- 694 [21] C. F. Cho *et al.*, "Blood-brain-barrier spheroids as an in vitro screening platform for brain-penetrating  
695 agents," *Nat. Commun.*, vol. 8, pp. 1–14, 2017.
- 696 [22] E. Urich, C. Patsch, S. Aigner, M. Graf, R. Iacone, and P. O. Freskgård, "Multicellular self-assembled  
697 spheroidal model of the blood brain barrier," *Sci. Rep.*, vol. 3, 2013.
- 698 [23] J. D. Wang, E. S. Khafagy, K. Khanafer, S. Takayama, and M. E. H. Elsayed, "Organization of  
699 Endothelial Cells, Pericytes, and Astrocytes into a 3D Microfluidic in Vitro Model of the Blood-Brain  
700 Barrier," *Mol. Pharm.*, vol. 13, no. 3, pp. 895–906, 2016.
- 701 [24] R. Booth and H. Kim, "Characterization of a microfluidic in vitro model of the blood-brain barrier  
702 ( $\mu$ BBB)," *Lab Chip*, vol. 12, no. 10, p. 1784, 2012.
- 703 [25] H. Cho *et al.*, "Three-Dimensional Blood-Brain Barrier Model for in vitro Studies of Neurovascular  
704 Pathology," *Sci. Rep.*, vol. 5, p. 15222, 2015.
- 705 [26] H. Xu *et al.*, "A dynamic in vivo-like organotypic blood-brain barrier model to probe metastatic brain  
706 tumors," *Sci. Rep.*, vol. 6, no. 1, p. 36670, 2016.
- 707 [27] A. Herland, A. D. van der Meer, E. A. FitzGerald, T.-E. Park, J. J. F. Sleeboom, and D. E. Ingber,  
708 "Distinct Contributions of Astrocytes and Pericytes to Neuroinflammation Identified in a 3D Human  
709 Blood-Brain Barrier on a Chip," *PLoS One*, vol. 11, no. 3, p. e0150360, 2016.
- 710 [28] I. M. Braverman, "The Cutaneous Microcirculation," *J. Investig. Dermatology Symp. Proc.*, vol. 5,  
711 no. 1, pp. 3–9, 2000.
- 712 [29] A. D. Wong, M. Ye, A. F. Levy, J. D. Rothstein, D. E. Bergles, and P. C. Searson, "The blood-brain  
713 barrier: an engineering perspective," *Front. Neuroeng.*, vol. 6, no. August, pp. 1–22, 2013.
- 714 [30] T. Takano *et al.*, "Astrocyte-mediated control of cerebral blood flow.," *Nat. Neurosci.*, vol. 9, no. 2,  
715 pp. 260–267, 2006.
- 716 [31] K. Kisler, A. R. Nelson, A. Montagne, and B. V. Zlokovic, "Cerebral blood flow regulation and  
717 neurovascular dysfunction in Alzheimer disease," *Nat. Rev. Neurosci.*, vol. 18, no. 7, pp. 419–434,  
718 2017.
- 719 [32] G. Adriani, D. Ma, A. Pavesi, and R. D. Kamm, "A 3D neurovascular microfluidic model consisting  
720 of neurons, astrocytes and cerebral endothelial cells as a blood-brain barrier," *Lab Chip*, vol. 12, pp.  
721 169–182, 2017.
- 722 [33] J. A. Whisler, M. B. Chen, and R. D. Kamm, "Control of perfusable microvascular network

- 723 morphology using a multiculture microfluidic system.," *Tissue Eng. Part C. Methods*, vol. 20, no. 7,  
724 pp. 543–52, 2014.
- 725 [34] S. Bang *et al.*, "A Low Permeability Microfluidic Blood-Brain Barrier Platform with Direct Contact  
726 between Perfusable Vascular Network and Astrocytes," *Sci. Rep.*, vol. 7, no. 1, p. 8083, 2017.
- 727 [35] E. a Winkler, R. D. Bell, and B. V Zlokovic, "Central nervous system pericytes in health and  
728 disease.," *Nat. Neurosci.*, vol. 14, no. 11, pp. 1398–1405, 2011.
- 729 [36] Y. Shin *et al.*, "Reconstituting vascular microenvironment of neural stem cell niche in three-  
730 dimensional extracellular matrix," *Adv. Healthc. Mater.*, vol. 3, no. 9, pp. 1457–1464, 2014.
- 731 [37] Y. Shin *et al.*, "Microfluidic assay for simultaneous culture of multiple cell types on surfaces or  
732 within hydrogels," *Nat. Protoc.*, vol. 7, no. 7, pp. 1247–1259, 2012.
- 733 [38] A. Hasan *et al.*, "Microfluidic techniques for development of 3D vascularized tissue," *Biomaterials*,  
734 vol. 35, no. 26, pp. 7308–7325, 2014.
- 735 [39] K. Haase and R. D. Kamm, "Advances in on-chip vascularization.," *Regen. Med.*, vol. 12, no. 3, pp.  
736 285–302, 2017.
- 737 [40] F. E. Curry, V. H. Huxley, and R. H. Adamson, "Permeability of single capillaries to intermediate-  
738 sized colored solutes.," *Am. J. Physiol.*, vol. 245, no. 3, pp. H495-505, 1983.
- 739 [41] D. G. Belair *et al.*, "Human vascular tissue models formed from human induced pluripotent stem cell  
740 derived endothelial cells," *Stem Cell Rev. Reports*, vol. 11, no. 3, pp. 511–525, 2015.
- 741 [42] S. Kim, H. Lee, M. Chung, and N. L. Jeon, "Engineering of functional, perfusable 3D microvascular  
742 networks on a chip," *Lab Chip*, vol. 13, no. 8, pp. 1489–1500, 2013.
- 743 [43] and R. D. K. Michelle B. Chen, Jordan A. Whisler , Jessie S. Jeon, "Mechanisms of tumor cell  
744 extravasation in an in vitro microvascular network platform," *Integr. Biol.*, vol. 144, no. 5, pp. 724–  
745 732, 2014.
- 746 [44] J. S. Jeon *et al.*, "Generation of 3D functional microvascular networks with human mesenchymal  
747 stem cells in microfluidic systems," *Integr. Biol.*, vol. 6, no. 5, pp. 555–563, 2014.
- 748 [45] T. Osaki, Y. Shin, V. Sivathanu, M. Campisi, and R. D. Kamm, "In Vitro Microfluidic Models for  
749 Neurodegenerative Disorders," *Adv. Healthc. Mater.*, vol. 1700489, p. 1700489, 2017.
- 750 [46] P. Kreczmanski *et al.*, "Microvessel length density, total length, and length per neuron in five  
751 subcortical regions in schizophrenia," *Acta Neuropathol.*, vol. 117, no. 4, pp. 409–421, 2009.
- 752 [47] B. Obermeier, R. Daneman, and R. M. Ransohoff, "Development, maintenance and disruption of the  
753 blood-brain-barrier," *Nat. Med.*, vol. 19, no. 12, pp. 1584–1596, 2013.
- 754 [48] N. Hagan and A. Ben-Zvi, "The molecular, cellular, and morphological components of blood-brain  
755 barrier development during embryogenesis," *Semin. Cell Dev. Biol.*, vol. 38, pp. 7–15, 2015.
- 756 [49] R. Daneman, L. Zhou, A. A. Kebede, and B. A. Barres, "Pericytes are required for blood-brain barrier  
757 integrity during embryogenesis," *Nature*, vol. 468, no. 7323, pp. 562–566, 2010.
- 758 [50] G. Bergers and S. Song, "The role of pericytes in blood-vessel formation and maintenance.," *Neuro.*

- 759 *Oncol.*, vol. 7, no. 4, pp. 452–464, 2005.
- 760 [51] M. A. Proescholdt *et al.*, “Vascular endothelial growth factor (VEGF) modulates vascular  
761 permeability and inflammation in rat brain,” *J. Neuropathol. Exp. Neurol.*, 1999.
- 762 [52] J. Kim, M. Chung, S. Kim, D. H. Jo, J. H. Kim, and N. L. Jeon, “Engineering of a biomimetic  
763 pericyte-covered 3D microvascular network,” *PLoS One*, vol. 10, no. 7, pp. 1–15, 2015.
- 764 [53] R. C. Brown, A. P. Morris, and R. G. O’Neil, “Tight junction protein expression and barrier  
765 properties of immortalized mouse brain microvessel endothelial cells,” *Brain Res.*, vol. 1130, no. 1,  
766 pp. 17–30, 2007.
- 767 [54] M. D. Sweeney, S. Ayyadurai, and B. V. Zlokovic, “Pericytes of the neurovascular unit: key functions  
768 and signaling pathways,” *Nat. Neurosci.*, vol. 19, no. 6, pp. 771–83, 2016.
- 769 [55] B. Prabhakarparandian *et al.*, “SyM-BBB: a microfluidic Blood Brain Barrier model,” *Lab Chip*, vol.  
770 13, no. 6, pp. 1093–1101, 2013.
- 771 [56] W. Löscher and H. Potschka, “Blood-brain barrier active efflux transporters: ATP-binding cassette  
772 gene family,” *NeuroRX*, vol. 2, no. 1, pp. 86–98, 2005.
- 773 [57] S. Banerjee and M. A. Bhat, “Neuron-Glial Interactions in Blood-Brain Barrier Formation,” *Annu.*  
774 *Rev. Neurosci.*, vol. 30, pp. 235–258, 2007.
- 775 [58] S.-W. Lee *et al.*, “SSeCKS regulates angiogenesis and tight junction formation in blood-brain  
776 barrier,” *Nat. Med.*, vol. 9, no. 7, pp. 900–906, 2003.
- 777 [59] D. J. Begley, “Delivery of therapeutic agents to the central nervous system: the problems and the  
778 possibilities,” *Pharmacol. Ther.*, vol. 104, no. 1, pp. 29–45, 2004.
- 779 [60] W. Yuan, Y. Lv, M. Zeng, and B. M. Fu, “Non-invasive measurement of solute permeability in  
780 cerebral microvessels of the rat,” *Microvasc. Res.*, vol. 77, no. 2, pp. 166–173, Mar. 2009.
- 781 [61] S. Y. Shi L., Zeng M., “Quantification of Blood-Brain Barrier Solute Permeability and Brain  
782 Transport by Multiphoton Microscopy,” vol. 136, no. March 2014, pp. 1–9, 2014.
- 783 [62] Y. I. Wang, H. E. Abaci, and M. L. Shuler, “Microfluidic blood-brain barrier model provides in vivo-  
784 like barrier properties for drug permeability screening,” *Biotechnol. Bioeng.*, vol. 114, no. 1, pp. 184–  
785 194, 2017.
- 786 [63] S. G. Canfield *et al.*, “An isogenic blood-brain model comprising brain endothelial cells, astrocytes  
787 and neurons derived from human induced pluripotent stem cells,” *Neurochem. J. O F*, no. 140, pp.  
788 874–888, 2017.
- 789 [64] J. M. Guanglei Li, Melissa J. Simon, Limary M. Cancel, Zhong-Dong Shi, Xinying Ji and and B. M.  
790 F. Tarbell, Barclay Morrison, “Permeability of Endothelial and Astrocyte Cocultures: In Vitro Blood-  
791 Brain Barrier Models for Drug Delivery Studies,” *Annu. Biomed. Eng.*, vol. 38, no. 8, pp. 2499–2511,  
792 2010.
- 793 [65] J. D. Huber, K. A. Witt, S. Hom, R. D. Egleton, K. S. Mark, and T. P. Davis, “Inflammatory pain  
794 alters blood-brain barrier permeability and tight junctional protein expression,” *Am. J. Physiol. Heart*

- 795 *Circ. Physiol.*, vol. 280, no. 3, pp. H1241–H1248, 2001.
- 796 [66] A. Appelt-Menzel *et al.*, “Establishment of a Human Blood-Brain Barrier Co-culture Model  
797 Mimicking the Neurovascular Unit Using Induced Pluri- and Multipotent Stem Cells,” *Stem Cell*  
798 *Reports*, vol. 8, no. 4, pp. 894–906, 2017.
- 799 [67] M. W. Toepke and D. J. Beebe, “PDMS absorption of small molecules and consequences in  
800 microfluidic applications,” *Lab Chip*, no. c, pp. 1484–1486, 2006.
- 801 [68] E. Ostuni, C. S. Chen, D. E. Ingber, and G. M. Whitesides, “Selective Deposition of Proteins and  
802 Cells in Arrays of Microwells,” *Langmuir*, vol. 17, no. 9, pp. 2828–2834, 2001.
- 803 [69] A. Gokaltun, M. L. Yarmush, A. Asatekin, and O. B. Usta, “Recent advances in nonbiofouling PDMS  
804 surface modification strategies applicable to microfluidic technology,” *Technology*, vol. 5, no. 1, pp.  
805 1–12, 2017.
- 806 [70] S. Jon, J. Seong, A. Khademhosseini, T. T. Tran, P. E. Laibinis, and R. Langer, “Construction of  
807 Nonbiofouling Surface by Polymeric Self-Assembled Monolayers,” *Langmuir*, vol. 19, no. 24, pp. 0–  
808 4, 2003.
- 809 [71] L. Cucullo, M. Hossain, V. Puvenna, N. Marchi, and D. Janigro, “The role of shear stress in Blood-  
810 Brain Barrier endothelial physiology,” *BMC Neurosci.*, vol. 12, no. 1, p. 40, 2011.
- 811 [72] C. Hajal *et al.*, “In vitro models of molecular and nano-particle transport across the blood-brain  
812 barrier In vitro models of molecular and nano-particle transport across the blood-brain barrier,”  
813 *Biomicrofluidics*, vol. 42213, no. 12, 2018.
- 814 [73] M. B. Chen, J. A. Whisler, J. Fröse, C. Yu, Y. Shin, and R. D. Kamm, “On-chip human  
815 microvasculature assay for visualization and quantification of tumor cell extravasation dynamics,”  
816 *Nat. Protoc.*, vol. 12, no. 5, pp. 865–880, 2017.

817

818

819 **Acknowledgements**

820

821 M.C. was supported by Ermenegildo Zegna Founder's scholarship and then by the MIT-POLITO  
822 grant (BIOMODE - Compagnia di San Paolo) under the joint "Doctorate of Bioengineering and  
823 Medical-Surgical Sciences" of University of Turin and Politecnico di Torino. Y.S. and R.K. were  
824 supported by grants from the Cure Alzheimer's Fund. T.O. was supported by research fellow overseas  
825 (Japan Society for the Promotion of Science). R.K. and T.O. also acknowledge the support of National  
826 Science Foundation for a Science and Technology Center on Emergent Behaviors of Integrated  
827 Cellular Systems, (CBET-0939511). C.H. and R.K. were supported by the National Cancer Institute  
828 (U01 CA202177). M.C., V.C., and R.K. also acknowledge the support of the research collaborations  
829 and exchanges program between MIT and POLITO (MITOR project NANOCAB).

830

831 **Author contributions**

832

833 All authors designed the experiments. M.C. performed majority of experiments, analyzed all data,  
834 and wrote the manuscript. Y.S. designed the microfluidic device and highly contributed to perform  
835 immunocytochemistry, permeability assays and vascular parameters analysis. T.O. designed and  
836 contributed to RT-PCR experiments, schematic drawings of this paper, statistical tests, discussion  
837 and writing of the manuscript. C.H. and M.C. performed vascular parameters analysis. R.K. and V.C.  
838 co-supervised the project. V.C. provided inputs in the writing of the manuscript. R.K. provided  
839 critical inputs to the experimental design and writing of the manuscript. All authors reviewed and  
840 accepted the manuscript.

841

842 **Additional information**

843

844 **Competing financial interests**

845 R.K. is co-founder and has a significant financial interest in AIM Biotech, a company that

846 manufactures microfluidic systems.